Supplemental Information

648 Hilbert space dimensionality in biphoton frequency combs: entanglement of formation and Schmidt mode decomposition

Kai-Chi Chang[1,+,*], Xiang Cheng[1,+], Murat Can Sarihan[1], Abhinav Kumar Vinod[1], Yoo Seung Lee[1], Tian Zhong[2], Yan-Xiao Gong[3], Zhenda Xie[4], Jeffrey H. Shapiro[5], Franco N. C. Wong[5], and Chee Wei Wong[1,*]

[1] Fang Lu Mesoscopic Optics and Quantum Electronics Laboratory, Department of Electrical and Computer Engineering & Center for Quantum Science and Engineering, University of California, Los Angeles, CA 90095, USA

[2] Institute for Molecular Engineering, University of Chicago, Chicago, Illinois 60637, USA

[3] National Laboratory of Solid State Microstructures and School of Physics, Nanjing University, Nanjing 210093, PR China

[4] National Laboratory of Solid State Microstructures and School of Electronic Science and Engineering, Nanjing University, Nanjing 210093, PR China

[5] Research Laboratory of Electronics, Massachusetts Institute of Technology, Cambridge, MA 02139, USA

+ equal contribution

* email: uclakcchang@ucla.edu; cheewei.wong@ucla.edu

In this Supplemental Information, we provide detailed theoretical calculations behind the experimental results presented in the main text, as well as additional information about the experimental implementations. In Sections I and II, respectively, we present the theories of Hong-Ou-Mandel (HOM) and Franson interferometry and use them to quantify their interference recurrences when they are illuminated by a biphoton frequency comb (BFC) [S1-S11]. These sections also include some experimental results, viz., HOM interference recurrences produced by the 5.03 GHz free-spectral range (FSR) cavity BFC, and Franson interference fringe patterns at seven different recurrences obtained using the 45.32 GHz BFC. In Section III, we use the Franson interference recurrences from the main text's Figure 4 to calculate lower bounds on the entanglements of formation (E_{of}) for the BFCs created using our 45.32 GHz and 15.15 GHz cavities [S12- S14]. In Section IV, we extract the frequency-binned and time-binned Schmidt eigenvalues and Schmidt numbers [S15, S16] from the main text's frequency-bin correlations and HOM-interference recurrences. Finally, in Section V, we exhibit a mixed state of entangled frequency pairs that has a symmetric joint-spectral amplitude (JSA) and the same joint-spectral intensity (JSI) as our BFC. We then use the theory of conjugate-Franson interferometry [S17] to show that its interference recurrences distinguish that mixed state from our BFC and thus can provide a definitive demonstration of BFC generation.

Supplementary Discussion I

First, we discuss the theory of Hong-Ou-Mandel interference produced by biphoton frequency combs. HOM interference quantifies the distinguishability of a pair of photons [S18]. Previous experiments [S19- S21], as well as this paper's main text, have observed HOM-interference recurrences from a cavity-filtered, continuous-wave (cw) pumped, spontaneous parametric downconverter (SPDC) source. As explained in the main text, theory predicts that this process will produce a BFC. Here we will present the theory of the HOM interference recurrences that result from such BFC illumination.

Quantum interference occurs in our HOM interferometer's 50:50 fiber coupler. For an ideal 50:50 fiber coupler, the field operators at detectors D_1 and D_2 are

$$\hat{E}_1(t) = \frac{1}{\sqrt{2}}\left[\hat{E}_S(t) + \hat{E}_I(t+\delta T)\right],\ \hat{E}_2(t) = \frac{1}{\sqrt{2}}\left[\hat{E}_S(t) - \hat{E}_I(t+\delta T)\right], \tag{1}$$

where the signal (S) and idler (I) field operators entering the coupler are given by

$$\hat{E}_K(t) = \frac{1}{\sqrt{2\pi}}\int d\omega\, \hat{a}_K(\omega)e^{-i\omega t}, \tag{2}$$

and δT is the HOM interferometer's relative arrival-time delay. We can write the biphoton coincidence rate as

$$R_{12} \propto \int d\tau G_{12}^{(2)}(t, t+\tau), \tag{3}$$

where the second-order correlation function is given by

$$G_{12}^{(2)}(t, t+\tau) = \left|\langle 0|\hat{E}_1(t)\hat{E}_2(t+\tau)|\psi\rangle\right|^2, \tag{4}$$

with $|\psi\rangle$ being the BFC state. For the following calculations, we assume ideal cw pumping. Then, substituting Eqs. (1) and (2) into Eq. (4), we obtain

$$G_{12}^{(2)}(t, t+\tau) \propto |\psi(\tau+\delta T) - \psi(-\tau+\delta T)|^2 \tag{5}$$

where $\Psi(t) \equiv \int \Phi(\Omega)\ e^{i\Omega t} d\Omega$ is the BFC state's (unnormalized) joint-temporal amplitude (JTA), and $\Phi(\Omega)$ is its (unnormalized) joint-spectral amplitude (JSA). By evaluating Eq. (3), we obtain the coincidence rate

$$R_{12} \propto 1 - \frac{\mathrm{Re}[\int \Phi^*(-\Omega)\Phi(\Omega)e^{2i\Omega\delta T}d\Omega]}{\int |\Phi(\Omega)|^2 d\Omega}. \tag{6}$$

For our BFC source, $\Phi(\Omega)$ has the following form

$$\Phi(\Omega) = \sum_m f'(\Omega)h(\Omega)f(\Omega - m\Delta\Omega), \tag{7}$$

where $f'(\Omega) = \mathrm{sinc}(A\Omega)$ is the phase-matching function, with full-width-at-half-maximum (FWHM) bandwidth $B_{PM} = 2.78/2\pi A$. Fiber Bragg grating's rectangular filter function is $h(\Omega) = \mathrm{rect}(\Omega/B)$, with B being its bandwidth. To compare theory with the main text's Figure 1b, i.e., its 45.32 GHz cavity HOM interference recurrences, we use the following parameter values: $A = 181$ ps, $B/2\pi = 346$ GHz, $\Delta\Omega/2\pi = 45.32$ GHz, and $\Delta\omega/\pi = 1.563$ GHz. In what follows, we will neglect the frequency-bin overlaps in $\Phi(\Omega)$, because $\Delta\Omega \gg \Delta\omega$, and so we obtain the following result for the BFC's (unnormalized) joint-spectral intensity (JSI),

$$|\Phi(\Omega)|^2 = \sum_{m=-N_0}^{N_0} \frac{\mathrm{sinc}^2(A\Omega)}{[(\Delta\omega)^2 + (\Omega - m\Delta\Omega)^2]^2}, \tag{8}$$

where $N_0 = [B/2\Delta\Omega]$ is the integer part of $B/2\Delta\Omega$. Furthermore, because $B > B_{PM} \gg \Delta\omega$, we can reduce Eq. (8) to

$$|\Phi(\Omega)|^2 \cong \sum_{m=-N_0}^{N_0} \frac{\mathrm{sinc}^2(Am\Delta\Omega)}{[(\Delta\omega)^2 + (\Omega - m\Delta\Omega)^2]^2}. \tag{9}$$

From this result we then find that

$$\int |\Phi(\Omega)|^2 d\Omega = \frac{\pi}{2(\Delta\omega)^3} \sum_{m=-N_0}^{N_0} \mathrm{sinc}^2(Am\Delta\Omega) \tag{10}$$

and

$$\int \Phi^*(-\Omega)\Phi(\Omega)e^{2i\Omega\delta T}d\Omega$$
$$= \frac{\pi e^{-2\Delta\omega|\delta T|}(1 + 2\Delta\omega|\delta T|)}{2(\Delta\omega)^3}\left[\sum_{m=-N_0}^{N_0} \mathrm{sinc}^2(Am\Delta\Omega)\cos(2m\Delta\Omega\delta T)\right]. \tag{11}$$

Combining Eqs. (11) and (6), we get our final theoretical result for the BFC HOM interference recurrences,

$$R_{12} \propto 1 - \frac{e^{-2\Delta\omega|\delta T|}(1+2\Delta\omega|\delta T|)}{\sum_{m=-N_0}^{N_0}\mathrm{sinc}^2(Am\Delta\Omega)}\left[\sum_{m=-N_0}^{N_0}\mathrm{sinc}^2(Am\Delta\Omega)\cos(2m\Delta\Omega\delta T)\right]. \tag{12}$$

The normalized theoretical coincidence rate for the BFC generated using our 45.32 GHz cavity is plotted for -340 ps $\leq \delta T \leq$ 340 ps in Supplementary Figure 1. Here we see interference recurrences with an ≈11.02 ps period, which matches well with the 11.03 ps period found in our measurements. The linewidth of each HOM-interference recurrence and its visibility fall-off for time bins farther away from zero relative delay also match with our measurements.

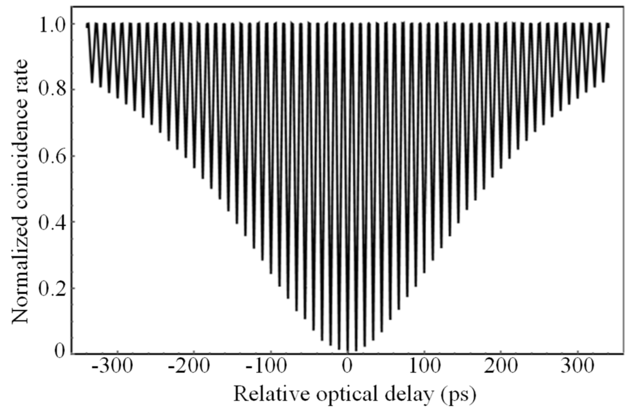

Supplementary Figure 1 | Modeling of the HOM-interference recurrences for the 45.32 GHz BFC. The normalized theoretical coincidence rate as a function of relative optical delay between the signal and idler photons. There are 61 interference recurrences for the whole optical-delay scanning range. The visibility decay away from zero relative delay arises from the Lorentzian lineshape of cw-pumped SPDC photons filtered by a fiber cavity.

We also calculated the HOM-interference recurrences for the 5.03 GHz fiber cavity BFC using the following parameter values: $A = 1.81$ ps, $B/2\pi = 346$ GHz, $\Delta\Omega/2\pi = 5.03$ GHz, and $\Delta\omega/\pi = 0.457$ GHz. The result, plotted in Supplementary Figure 2, is consistent with the experimental data shown in Supplementary Figure 3. We see that there are fewer interference fringes compared to those in Supplementary Figure 1, which is a consequence of the 5.03 GHz cavity's smaller FSR, and the ≈ 99.6 ps recurrence period matches well with the 99.4 ps period seen in our measurements.

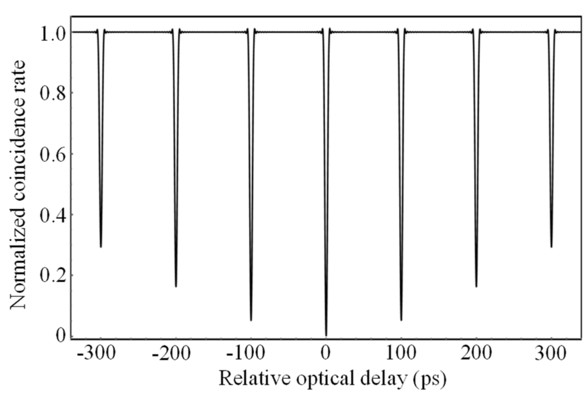

Supplementary Figure 2 | Modeling of the HOM-interference recurrences for the 5.03 GHz

BFC. The normalized theoretical coincidence rate as a function of relative optical delay. There are 7 interference recurrences for the whole optical-delay scanning range in Supplementary Figure 2, which agrees well with the experimental results shown in Supplementary Figure 3.

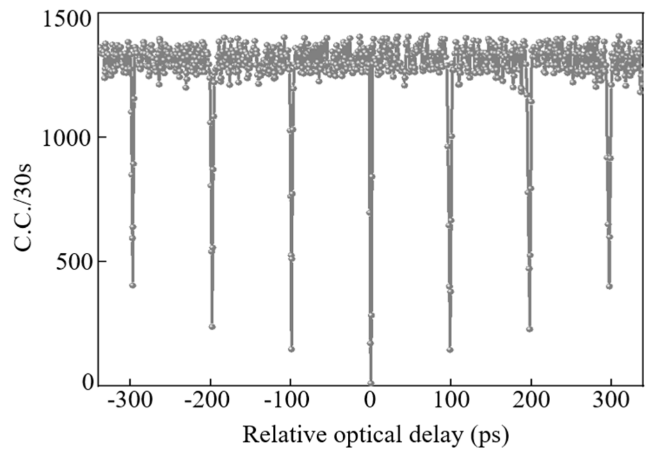

Supplementary Figure 3 | Experimental HOM-interference recurrences for the 5.03 GHz BFC. Coincidence counts versus relative optical delay between the two arms of the HOM interferometer. A total of 7 HOM-interference recurrences are observed.

The visibilities of the HOM-interference recurrences drop less rapidly in Supplementary Figure 2 compared to what is seen in Supplementary Figure 1 – despite 5.03 GHz cavity's lower finesse of ≈ 10 – because of the limited scan range of the relative optical delay for observing the recurrence visibilities' fall-off.

Supplementary Discussion II

Following the discussion of HOM interference of biphoton frequency combs, here, we present the theory of Franson interference of such high-dimensional source. In Franson interferometry's two unbalanced Mach-Zehnder interferometers (MZIs), the field operators at their respective detectors, D_1 and D_2, are

$$\hat{E}_1(t) = \frac{1}{\sqrt{2}}\left[\hat{E}_S(t) + \hat{E}_S(t - \Delta T_1)\right],\ \hat{E}_2(t) = \frac{1}{\sqrt{2}}\left[\hat{E}_I(t) - \hat{E}_I(t - \Delta T_2)\right], \tag{13}$$

where the signal (S) and idler (I) field operators entering the Franson interferometer, $\hat{E}_K(t)$ for $K = S, I$, are given by

$$\hat{E}_K(t) = \frac{1}{\sqrt{2\pi}} \int d\omega\, \hat{a}_K(\omega) e^{-i\omega t}. \tag{14}$$

Here, ΔT_1 and ΔT_2 – the delay differences between each MZI's long and short paths – are sufficient to ensure that there is no long-short second-order interference. We can write the biphoton coincidence rate as

$$R_{12} \propto \int d\tau G_{12}^{(2)}(t, t+\tau), \tag{15}$$

where

$$G_{12}^{(2)}(t, t+\tau) = \left|\langle 0|\hat{E}_1(t)\hat{E}_2(t+\tau)|\psi\rangle\right|^2, \tag{16}$$

with $|\psi\rangle$ being the BFC state. For the following calculations, we assume ideal cw pumping. Then, substituting Eqs. (13) and (14) into Eq. (16) and suppressing the terms representing long-short path interference, we get

$$G_{12}^{(2)}(t, t+\tau) = \left|\Psi(\tau) + \Psi(\tau - \delta T)e^{\frac{-i\omega_p(\Delta T_1 + \Delta T_2)}{2}}\right|^2, \tag{17}$$

where, as before, $\Psi(t) = \int \Phi(\Omega)\ e^{i\Omega t} d\Omega$ is the BFC's JTA, $\Phi(\Omega)$ is its JSA, and

$$\delta T = \Delta T_1 - \Delta T_2, \tag{18}$$

By evaluating Eq. (15), we obtain the coincidence rate

$$R_{12} \propto 1 + |\Gamma(\delta T)| \cos(\tfrac{\omega_p \delta T}{2} + \omega_p \Delta T_2 + \varphi). \tag{19}$$

where $\Gamma(\delta T) = \int |\Phi(\Omega)|^2 e^{i\Omega\delta T} \,/\, \int |\Phi(\Omega)|^2 d\Omega$, and

$$\Gamma(\delta T) = |\Gamma(\delta T)| e^{i\varphi}. \tag{20}$$

For our BFC source, $\Phi(\Omega)$ is given by Eq. (11), thus we obtain

$$\int |\Phi(\Omega)|^2 e^{i\Omega\delta T} d\Omega$$
$$= \frac{\pi e^{-\Delta\omega|\delta T|}(1 + \Delta\omega|\delta T|)}{2(\Delta\omega)^3}\left[2\sum_{m=1}^{N_0} \mathrm{sinc}^2(Am\Delta\Omega)\cos(m\Delta\Omega\delta T) + 1\right]. \tag{21}$$

Combining Eqs. (19) and (21), we get our final theoretical result for the BFC's Franson interference recurrences,

$$R_{12} \propto 1 + \frac{e^{-\Delta\omega|\Delta T|}(1 + 2\Delta\omega|\delta T|)}{\sum_{m=-N_0}^{N_0} \mathrm{sinc}^2(Am\Delta\Omega)}\left[2\sum_{m=1}^{N_0} \mathrm{sinc}^2(Am\Delta\Omega)\cos(m\Delta\Omega\delta T) + 1\right]$$
$$\times \cos\left[\omega_p\left(\frac{\delta T}{2} + \Delta T_2\right)\right]. \tag{22}$$

We can model our experimental results with the theoretical parameters above and the experiment's ΔT_2 = 4.84 ns. The Franson interference visibility for the BFC generated using our 45.32 GHz cavity is plotted for -340 ps ≤ $\delta T \leq$ 340 ps in Supplementary Figure 4. Here we see an interference-recurrence pattern with an ≈ 22.1 ps period, which matches well with the 22.09 ps period found in our measurements in both main text and supplemental information. The width of each Franson recurrence and the fall-off in visibility for time bins increasingly far from zero delay also match with the experimental observations.

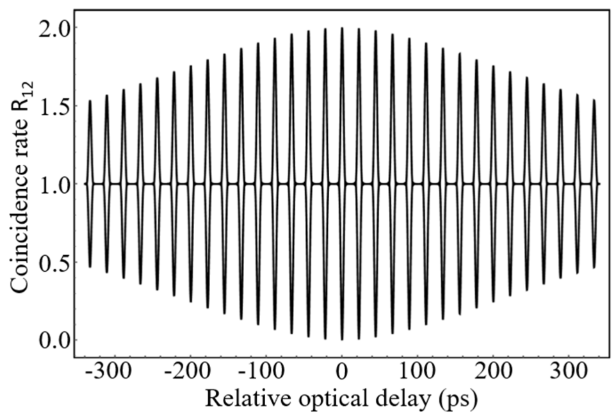

Supplementary Figure 4 | Modeling of the Franson interference recurrences for the 45.32 GHz BFC. Theoretical fringe envelope of Franson interference for the BFC generated using the 45.32 GHz fiber cavity. There are 31 recurrences for the whole optical-delay scanning range in which we have measured 16 time-bins, limited by our optical delay tuning range. The fall-off in the coincidence rate away from zero delay arises from the Lorentzian lineshape of the SPDC-generated photons after they have passed through the fiber cavity.

In Supplementary Figure 5 we present Franson interference fringes at relative delays ΔT_2 equal to 0, 3, 5, 7, 9, 11, 13, and 15 cavity round-trip times for the 45.32 GHz BFC.

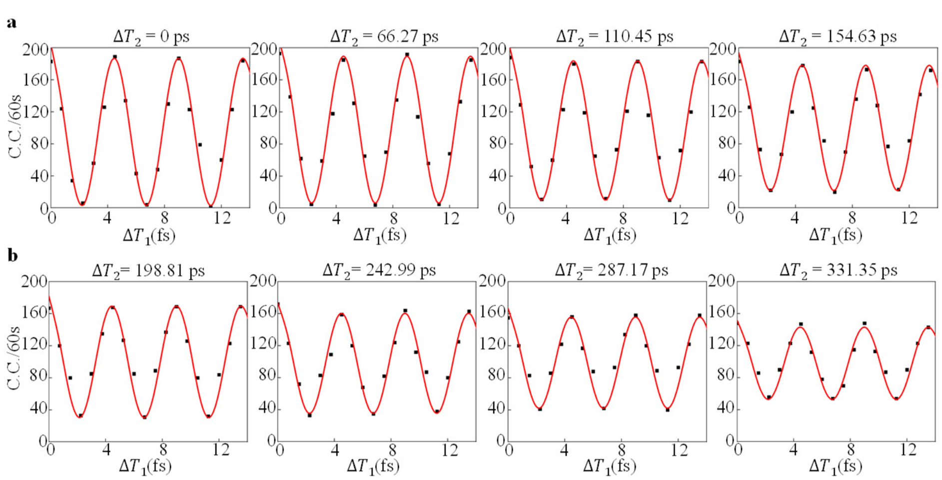

Supplementary Figure 5 | Franson interference fringes for the 45.32 GHz BFC. a, and **b,**

Measured Franson interference fringes as a function of ΔT_1, when ΔT_2 is set to 0, 3, 5, 7, 9, 11, 13, and 15 cavity round-trip times. The fringe visibilities obtained from these data are compared to theory in Supplementary Table 1 and shown in the main text Figure 4d.

Supplementary Table 1 | Franson visibilities of the 45.32 GHz BFC for different optical delays.

Cavity round-trip time	Visibility V_{th} (theoretical)	Visibility V_{exp} (experimental)
0	100.0%	99.1%
3	95.9%	94.4%
5	90.2%	88.3%
7	83.2%	80.1%
9	75.6%	73.1%
11	68.0%	65.0%
13	60.5%	56.7%
15	53.4%	48.7%

Supplementary Discussion III

Standard perturbation theory [S22] predicts that a cw-pumped SPDC source produces pure-state (or nearly pure-state) biphotons and stabilized-cavity filtering of those biphotons will then yield nonseparable-state BFCs. Proceeding under that assumption – which, as explained in the main text, is supported by earlier pulse-pumped SPDC experiments by our team [S23, S24] – we can quantify, albeit conservatively, the entanglement of our BFCs from lower bounds on their entanglements of formation, i.e., their E_{of}s. In particular, following Refs. [12-14], we have that

$$E_{of} \geq -\log_2\left(1 - \frac{B_e^2}{2}\right), \tag{23}$$

for a time-binned BFC, where

$$B_e = \frac{2}{\sqrt{|C|}}\left(\sum_{\substack{(j,k)\in C\\ j<k}} |\langle j,j|\rho|k,k\rangle| - \sqrt{\langle j,k|\rho|j,k\rangle\langle k,j|\rho|k,j\rangle}\right), \tag{24}$$

with ρ being the time-binned state's density matrix, and $|j,k\rangle$ being the biphoton ket for the jth signal time bin and the kth idler time bin. Here, C is the set of time-bin indices used in the sum, with $|C|$ being that set's cardinality. This lower bound is useful even when we have access only to a submatrix of the density matrix. For a $d \times d$ submatrix, a maximally-entangled state has $B_e =$

$\sqrt{2(d-1)/d}$, leading to $E_{of} = \log_2(d)$ ebits. In our experimental setup, shown in the main text's Figure 4a, there were technical limitations that prevented our measuring all the elements of the BFC's full density matrix. These limitations were due to: (1) our Franson interferometer's only having a free-space motorized optical-delay line in its arm 2; and (2) that stage's 360 ps travel range being aligned with the 0$^{\text{th}}$ time-bin close to the stage's starting position. Thus, we measured only one side of the Franson interference revival time-bins.

To instantiate the bound from Eq. (23), we used the visibilities of our BFC's Franson interference recurrences for the $\langle j,k|\rho|j,k\rangle$ values. Supplementary Table 2 shows the resulting 3×3 submatrix elements for 45.32 GHz cavity's Franson interference. Here, the blue entries are measurements, the green entries follow from presuming our BFC has time-bin symmetry – as seen, e.g., in that BFC's HOM-interference recurrences – and the black entries are obtained by extrapolating the visibilities using the cavity's Lorentzian lineshape.

Supplementary Table 2 | Franson interference 3×3 submatrix elements for obtaining a lower bound on the entanglement of formation for the 45.32 GHz BFC.

Visibility	0$^{\text{th}}$ time-bin	1$^{\text{st}}$ time-bin	2$^{\text{nd}}$ time-bin
0$^{\text{th}}$ time-bin	**99.1%**	**98.3%**	**96.9%**
1$^{\text{st}}$ time-bin	**98.3%**	**99.1%**	**95.1%**
2$^{\text{nd}}$ time-bin	**96.9%**	**95.1%**	**99.1%**

Supplementary Table 3 shows the 45.32 GHz and 15.15 GHz cavities' E_{of} lower bounds for $d = 2$ to 4. They were obtained, using the procedure described for Supplementary Table 2, from the measured Franson interference visibilities in the main text's Figure 4d. Note that we chose not to go to higher d values here because increasing d makes the bounds increasingly dependent on submatrix elements derived from extrapolation rather than from direct measurements. Within that limited d range, our highest entanglements-of-formation lower bounds are $E_{of} \geq 1.89 \pm 0.03$ ebits for the 45.32 GHz cavity's BFC and $E_{of} \geq 1.40 \pm 0.05$ ebits for the 15.15 GHz cavity's BFC. Both were attained at $d = 4$, where 2 ebits corresponds to a maximally-entangled pure state of that dimensionality.

Supplementary Table 3 | Entanglements of formation lower bounds for the 45.32 GHz and the 15.15 GHz BFCs.

Dimension d	Maximum entangled ebits	ebits for 45.32 GHz BFC	ebits for 15.15 GHz BFC
2	1	0.98	0.93
3	1.58	1.54	1.30
4	2	1.89	1.40

Supplementary Discussion IV

In this section, we discuss the Schmidt eigenvalues and Schmidt numbers for frequency-binned and time-binned BFC states: experimental results versus theory. Supplementary Table 4 presents the Schmidt eigenvalues inferred from the frequency-bin correlation measurements shown in Figures 2b and 2c of the main text. They were obtained from performing a Schmidt decomposition on the frequency-correlation matrix [S25-S30]. In particular, with R_{jj} denoting the coincidence count for the signal's ith frequency bin and the idler's jth frequency bin, we diagonalized the matrix J_{Ω}, whose ijth element is ${R_{ij}}^{1/2}$. The Schmidt eigenvalues of the frequency-binned BFC state are the eigenvalues found from that diagonalization, and the Schmidt number they imply follows from Eq. (6) of the main text. For the following Supplementary Tables, we highlight and consider the dominant Schmidt modes that comprise over 60% of the total Schmidt eigenvalues for each measurement we have performed in the main text's Figure 2 (for the 45.32 GHz and 5.02 GHz cavities' BFCs) and Figure 2 of Ref. [S20] (for the 15.15 GHz cavity's BFC).

Supplementary Table 4 | Measured frequency-bin Schmidt eigenvalues and Schmidt numbers for the 45.32 GHz BFCs with pump powers ≈ 2 mW (left) and ≈ 4 mW (right). The dominant Schmidt eigenvalues are shown in boldface.

Number of frequency bins	Schmidt eigenvalues	Schmidt number	Number of frequency bins	Schmidt eigenvalues	Schmidt number
2	0.140	4.310	2	0.112	3.17
1	**0.218**		1	0.165	
0	**0.343**		0	0.499	
-1	**0.183**		-1	0.130	
-2	0.115		-2	0.091	

The results of performing the same frequency-bin Schmidt decomposition on the data we obtained for ≈ 2 mW pumping of the 15.15 GHz cavity setup is given in Supplementary Table 5. Here the 8.671 inferred Schmidt number is limited by the tunability of our 100 pm filters.

Supplementary Table 5 | Measured frequency-bin Schmidt eigenvalues and Schmidt number for the 15.15 GHz BFC and ≈ 2 mW pump power. The dominant Schmidt eigenvalues are shown in boldface.

Number of frequency bins	Schmidt eigenvalues	Schmidt number
4	0.084	8.67
3	0.100	
2	**0.114**	
1	**0.136**	
0	**0.147**	
-1	**0.128**	
-2	**0.109**	
-3	0.096	
-4	0.081	

The frequency-bin Schmidt decomposition for our 5.03 GHz BFC yielded the Schmidt eigenvalues and Schmidt number shown in Supplementary Table 6. The maximum possible Schmidt number for this measurement is 19, and our 11.67 result is mainly limited by the bandwidth and tunability of our 100 pm filters. Note that the results from Supplementary Tables 4 to 6 are also shown in Figure 5a of the main text.

Supplementary Table 6 | Measured frequency-bin Schmidt eigenvalues and Schmidt number for the 5.03 GHz BFC and ≈ 2 mW pump power. The dominant Schmidt eigenvalues are shown in boldface.

Number of frequency bins	Schmidt eigenvalues	Number of frequency bins	Schmidt eigenvalues	Schmidt number
9	0.020	**-1**	**0.101**	11.67
8	0.026	**-2**	**0.066**	
7	0.028	**-3**	**0.048**	
6	0.032	-4	0.039	
5	0.035	-5	0.033	
4	0.041	-6	0.030	
3	**0.052**	-7	0.027	
2	**0.074**	-8	0.023	
1	**0.114**	-9	0.013	
0	**0.190**			

For comparison purposes, and to derive our frequency-binned BFC's Hilbert-space dimensionality under ideal conditions, we conclude this section by presenting theoretical results for their Schmidt eigenvalues and their Schmidt numbers. According to main text's Eq. (7), we can write the BFC's frequency-binned JSI as:

$$|\psi(n_s\Delta\Omega, n_I\Delta\Omega)|^2 = \frac{\mathrm{sinc}^2(2.78 n_s\Delta\Omega/2\pi B_{PM})}{\sum_{n_s=-N_0}^{N_0}\mathrm{sinc}^2(2.78 n_s\Delta\Omega/2\pi B_{PM})}\delta_{n_s n_I}, \text{ for } -N_0 \le n_s, n_I \le N_0, \quad (25)$$

where $n_s\Delta\Omega$ is the positive detuning of the signal photon's radian frequency from degeneracy and $n_I\Delta\Omega$ is the negative detuning of the idler photon's radian frequency from degeneracy, and $\delta_{n_s n_I}$ is the Kronecker delta function. The J_Ω matrix, whose diagonalization provides the Schmidt eigenvalues, is then trivially obtained, because it is diagonal, and its diagonal elements,

$$\lambda_n = \frac{sinc^2(2.78 n_s \Delta\Omega / 2\pi B_{PM})}{\sum_{n_s=-N_0}^{N_0} sinc^2(2.78 n_s \Delta\Omega / 2\pi B_{PM})}, \text{ for } -N_0 \le n \le N_0, \tag{26}$$

are the Schmidt eigenvalues we are seeking. From these eigenvalues the theoretical Schmidt number for the frequency-binned BFC is therefore

$$K_\Omega = \left(\sum_{n=-N_0}^{N_0} \lambda_n^2\right)^{-1} = \frac{\left[\sum_{n_s=-N_0}^{N_0} \mathrm{sinc}^2(2.78 n_s \Delta\Omega / 2\pi B_{PM})\right]^2}{\sum_{n_s=-N_0}^{N_0} \mathrm{sinc}^4(2.78 n_s \Delta\Omega / 2\pi B_{PM})}. \tag{27}$$

Using the main text's Eq. (6), the theoretical Schmidt numbers for the frequency-binned BFC states are found to be 4.89, 20.21, and 34.39 for 45.32 GHz, 15.15 GHz, and 5.03 GHz FSR cavities, respectively. Hence the ideal Hilbert-space dimensionalities for frequency-binned BFCs scales with the FSR of the cavity used to generate that state.

We obtained our BFCs time-binned Schmidt eigenvalues from the visibilities of their measured HOM-interference recurrences via the procedure described in the main text. Supplementary Tables 7(a), 7(b) and 7(c) show the dominant Schmidt eigenvalues we found for the 45.32 GHz, 15.15 GHz, and 5.03 GHz BFCs. These results appear in the main text's Figure 5b.

Supplementary Table 7 | Measured dominant time-bin Schmidt eigenvalues for the BFCs generated using (a) the 45.32 GHz cavity, (b) the 15.15 GHz cavity, and (c) the 5.03 GHz cavity.

a

Number of time bins	Schmidt eigenvalues
4	0.045
3	0.056
2	0.070
1	0.087
0	0.109
-1	0.087
-2	0.070
-3	0.056
-4	0.045

b

Number of time bins	Schmidt eigenvalues
1	0.158
0	0.281
-1	0.158

c

Number of time bins	Schmidt eigenvalues
1	0.181
0	0.321
-1	0.180

Supplementary Discussion V

The main text and the Supplemental Information have presented compelling evidence of our having generated a 648-dimensional state under the presumption that cw-pumped SPDC followed by filtering through a highly-stabilized cavity produces a pure-state (or nearly pure-state) output. With the support from the presumption afforded by SPDC perturbation theory [S22] and our prior experimental work on unfiltered, pulse-pumped SPDC sources [S23, S24], and the new theoretical modeling of Conjugate Franson interferometry, we can support the purity of our high-dimensional BFC state. This section will introduce, for illustrative purposes, an entangled mixed state whose HOM-interference recurrences, frequency-bin correlations, and Franson interference recurrences are identical to those of the pure-state BFC. This mixed state, however, can be distinguished from the pure-state BFC via conjugate-Franson interferometry. First, we discuss the Pure-state versus mixed-state in filtered-SPDC measurements. Our pure-state BFC, in normalized form, is

$$|\psi_{\mathrm{BFC}}\rangle = \int \Phi_{\mathrm{BFC}}(\Omega)\hat{a}_H^{\dagger}\left(\frac{\omega_p}{2}+\Omega\right)\hat{a}_V^{\dagger}\left(\frac{\omega_p}{2}-\Omega\right)|0\rangle\, d\Omega\,, \tag{28}$$

where

$$\Phi_{\mathrm{BFC}}(\Omega) \propto \sum_{m=-N_0}^{N_0}\frac{\mathrm{sinc}(Am\Delta\Omega)}{(\Delta\omega)^2+(\Omega-m\Delta\Omega)^2} \tag{29}$$

with $\int|\Phi_{\mathrm{BFC}}(\Omega)|^2\, d\Omega = 1$. This state's JSI is therefore

$$\mathrm{JSI}_{\mathrm{BFC}}(\Omega) = |\Phi_{\mathrm{BFC}}(\Omega)|^2 = \sqrt{\frac{2\Delta\omega^3}{\pi}}\frac{\sum_{m=-N_0}^{N_0}\frac{\mathrm{sinc}^2(Am\Delta\Omega)}{[(\Delta\omega)^2+(\Omega-m\Delta\Omega)^2]^2}}{\sqrt{\sum_{n=-N_0}^{N_0}\mathrm{sinc}^2(An\Delta\Omega)}}\,. \tag{30}$$

It is obvious that the BFC's frequency-bin correlations are immediate consequences of its JSI. From Eq. (19), we see that the BFC's Franson interference recurrences are determined by that state's JSI. Finally, because $\Phi_{\mathrm{BFC}}(-\Omega) = \Phi_{\mathrm{BFC}}(\Omega)$, Eq. (6) shows that the BFC's HOM-interference recurrences are also determined by that state's JSI. Hence, entangled mixed states that possess this same JSI and a symmetric JSA cannot be distinguished from the BFC by means of any of the measurements we have performed. To illustrate that possibility, we now introduce the entangled frequency-pair state (EFS).

The EFS is an entangled mixed state whose density operator is

$$\hat{\rho}_{\mathrm{EFS}} = \sum_{m=0}^{N_0}\rho_{\mathrm{EFS}}(m)\left|\psi_{\mathrm{EFS}}^{(\mathrm{m})}\right\rangle\left\langle\psi_{\mathrm{EFS}}^{(\mathrm{m})}\right|, \tag{31}$$

where

$$|\psi_{\rm EFS}^{(\rm m)}\rangle \;=\; \int \Phi_{\rm EFS}^{(m)}(\Omega)\hat{a}_H^\dagger\left(\frac{\omega_p}{2}+\Omega\right)\hat{a}_V^\dagger\left(\frac{\omega_p}{2}-\Omega\right)|0\rangle\, d\Omega\,, \tag{32}$$

with

$$\Phi_{\rm EFS}^{(0)}(\Omega) \propto \frac{1}{(\Delta\omega)^2+\Omega^2}\,, \tag{33}$$

$$\Phi_{\rm EFS}^{(m)}(\Omega) \propto \frac{1}{\sqrt{2}}\left(\frac{{\rm sinc}(Am\Delta\Omega)}{(\Delta\omega)^2+(\Omega+m\Delta\Omega)^2}+\frac{{\rm sinc}(Am\Delta\Omega)}{(\Delta\omega)^2+(\Omega-m\Delta\Omega)^2}\right),\ \text{for } m=1,2,\ldots,N_0, \tag{34}$$

$\int|\Phi_{\rm EFS}^{(m)}(\Omega)|^2 d\Omega=1$, for all m, and the $\{\rho_{\rm EFS}(m)\}$ being a probability mass function that makes the EFS's JSI match that of the BFC state, i.e.,

$$\mathrm{JSI}_{\rm EFS}(\Omega)=\sum_{m=0}^{N_0}\rho_{\rm EFS}(m)\left|\Phi_{\rm EFS}^{(m)}(\Omega)\right|^2 \;=\; |\Phi_{\rm BFC}(\Omega)|^2 \;=\; \mathrm{JSI}_{\rm BFC}(\Omega). \tag{35}$$

Because the EFS and BFC have identical JSIs, their frequency-bin correlations and Franson interference recurrences will be indistinguishable. In addition, because $\Phi_{\rm BFC}(-\Omega)=\Phi_{\rm BFC}(\Omega)$ and $\Phi_{\rm EFS}^{(m)}(-\Omega)=\Phi_{\rm EFS}^{(m)}(\Omega)$, these two states will also have the same HOM-interference recurrences. Together, these results imply that our paper's measurements cannot distinguish between a BFC and the EFS that has the same JSI.

Next, we move on to the discussion of Conjugate-Franson interferometry, which was proposed in Ref. [S17] for security checking in time-frequency-entangled, high-dimensional quantum key distribution. The basic configuration for conjugate-Franson interferometry is shown in main text's Figure 6a. Conjugate-Franson interferometry of the BFC and the EFS turn out to have the following coincidence rates,

$$R_{12}^{\rm BFC}(\phi_S,\phi_I)\propto 1+\int d\Omega\,\mathrm{Re}\left[\Phi_{\rm BFC}^*(\Omega)\Phi_{\rm BFC}(\Omega-2\omega_m)e^{i(\phi_S+\phi_I)}\right], \tag{36}$$

and

$$R_{12}^{\rm EFS}(\phi_S,\phi_I)\propto 1+\sum_{m=0}^{N_0}\rho_{\rm EFS}(m)\int d\Omega\,\mathrm{Re}\left[\Phi_{\rm EFS}^{(m)*}(\Omega)\Phi_{\rm EFS}^{(m)}(\Omega-2\omega_m)e^{i(\phi_S+\phi_I)}\right], \tag{37}$$

where ϕ_S and ϕ_I are phase shifts incurred by wavelength-scale length differences between the two arms of each MZI. It is clear from Eqs. (36) and (37) that the conjugate-Franson interferometer's single-sideband modulation in one arm of each of its MZIs prevents their coincidence rates from being determined by their input states JSIs. Indeed, it is easily shown, from Eqs. (36) and (37), that these conjugate-Franson coincidence rates can be rewritten as

$$R_{12}^{\rm BFC}(\phi_S,\phi_I)\propto 1+\int d\tau\,\mathrm{JTI}_{\rm BFC}(\tau)\cos(\omega_m\tau+\phi_S+\phi_I), \tag{38}$$

and

$$R_{12}^{\text{EFS}}(\phi_S, \phi_I) \propto 1 + \int d\tau\, \text{JTI}_{\text{EFS}}(\tau) \cos(\omega_m \tau + \phi_S + \phi_I), \tag{39}$$

where the (normalized) joint-temporal intensities (JTIs) are given by $\text{JTI}_{\text{BFC}}(\tau) = |\Psi_{\text{BFC}}(\tau)|^2$ and $\text{JTI}_{\text{EFS}}(\tau) = \sum_{m=0}^{N_0} \rho_{\text{EFS}}(m) \left|\Psi_{\text{EFS}}^{(m)}(\tau)\right|^2$. Thus it is not surprising that conjugate-Franson interferometry should be able to discriminate between the BFC and the EFS even when they have identical JSIs.

The BFC only has appreciable conjugate-Franson interference at $\omega_m = |k|\Delta\Omega$ for $|k| = 1, 2, \dots, 2N_{0,}$ where its visibilities satisfy

$$V_{\text{BFC}}(k\Delta\Omega) = \frac{\sum_{m=-N_0}^{N_0-|k|} \text{sinc}(Am\Delta\Omega)\text{sinc}[A(m+|k|)\Delta\Omega}{\sum_{n=-N_0}^{N_0} \text{sinc}^2(An\Delta\Omega)}. \tag{40}$$

In contrast, the EFS has only appreciable conjugate-Franson interference at $|k| = 1, 2, \dots, 2N_{0,}$ where its visibilities obey

$$V_{BFC}(k\Delta\Omega)(k\Delta\Omega) = \frac{\text{sinc}^2(2Ak\Delta\Omega)}{\sum_{n=-N_0}^{N_0} \text{sinc}^2(An\Delta\Omega)}. \tag{41}$$

These results provide a clear and measurable signature for the BFC, as shown in the main text's Figures 6b and 6c for the 45.32 GHz BFC and its related EFS and in Supplementary Figures 6 and 7, for the 15.15 GHz cavity and 5.03 cavity cases respectively.

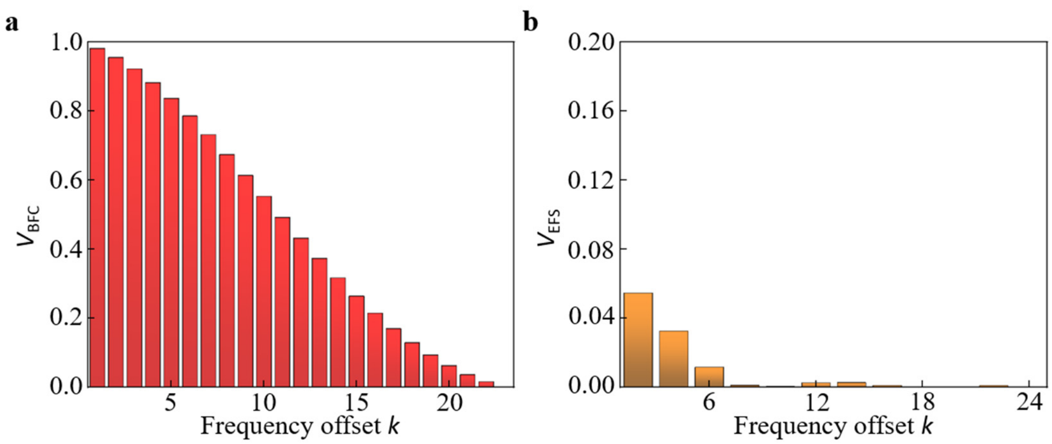

Supplementary Figure 6 | Visibilities of conjugate-Franson interference recurrences for the 15.15 GHz BFC and the EFS with the same JSI. (a) BFC conjugate-Franson interference has high-visibility recurrences and they occur only when the interferometer frequency offset is $k\Delta\Omega$

for integer k. **(b)** EFS conjugate-Franson interference has low-visibility recurrences and they only occur when the interferometer frequency offset is $2k\Delta\Omega$ for integer k.

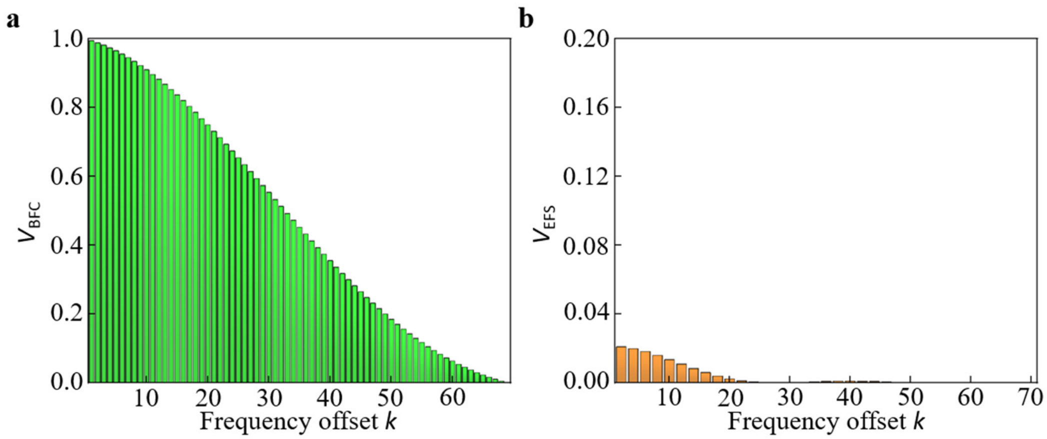

Supplementary Figure 7 | Visibilities of conjugate-Franson interference recurrences for the 5.03 GHz BFC and the EFS with the same JSI. (a) BFC conjugate-Franson interference has high-visibility recurrences and they occur only when the interferometer frequency offset is $k\Delta\Omega$ for integer k. **(b)** EFS conjugate-Franson interference has low-visibility recurrences and they only occur when the interferometer frequency offset is $2k\Delta\Omega$ for integer k.

Supplementary References

[S1] H. J. Carmichael, R. J. Glauber, and M. O. Scully, *Direction of quantum optics* (Springer, Berlin Heidelberg, 2001).

[S2] R. T. Thew, A. Acín, H. Zbinden, and N. Gisin, Bell-type test of energy-time entangled qutrits, *Phys. Rev. Lett.* **93**, 010503 (2004).

[S3] J. T. Barreiro, N. K. Langford, N. A. Peters, and P. G. Kwiat, Generation of hyperentangled photon pairs, *Phys. Rev. Lett.* **95**, 260501 (2005).

[S4] P. B. Dixon, G. A. Howland, J. Schneeloch, and J. C. Howell, Quantum Mutual Information Capacity for High-Dimensional Entangled States, *Phys. Rev. Lett.* **108**, 143603 (2012).

[S5] C. Eltschka and J. Siewert, Quantifying entanglement resources, *J. Phys. A.: Math. Theo.* **47**, 424005 (2014).

[S6] D. J. Lum, S. H. Knarr, and J. C. Howell, Fast Hadamard transforms for compressive sensing of joint systems: measurement of a 3.2 million-dimensional bi-photon probability distribution, *Opt. Express* **21**, 27636-27649 (2015).

[S7] M. Kues, et al. On-chip generation of high-dimensional entangled quantum states and their coherent control, *Nature* **546**, 622-626 (2017).

[S8] D. Cozzolino, B. D. Lio, D. Bacco, and L. K. Oxenløwe, High-dimensional quantum communication: benefits, progress, and future challenges, *Adv. Quantum Technol.* **2**, 1900038 (2019).
[S9] M. Erhard, R. Fickler, M. Krenn, and A. Zeilinger, Twisted photons: new quantum perspectives in high dimensions, *Light Sci. Appl.* **7**, 17146 (2018).
[S10] L. Lu, et al. Three-dimensional entanglement on a silicon chip, *npj Quantum Inf.* **6**, 1-9 (2020).
[S11] F. Brandt, M. Hiekkamäki, F. Bouchard, M. Huber, and R. Fickler, High-dimensional quantum gates using full-field spatial modes of photons, *Optica* **7**, 98-107 (2020).
[S12] A. Martin, et al. Quantifying photonic high-dimensional entanglement, *Phys. Rev. Lett.* **118**, 110501 (2017).
[S13] A. Tiranov, et al. Quantification of multidimensional entanglement stored in a crystal, *Phys. Rev. A* **96**, 040303 (2017).
[S14] P. Imany, et al. High-dimensional optical quantum logic in large operational spaces, *npj Quantum Inf.* **5**, 59 (2019).
[S15] F. Laudenbach, R. B. Jin, C. Greganti, M. Hentschel, P. Walther, and H. Hübel, Numerical investigation of photon-pair generation in periodically poled $M\mathrm{TiO}X\mathrm{O}_4$ (M = K, Rb, Cs; X = P, As), *Phys. Rev. Applied* **8**, 024035 (2017).
[S16] C. Chen, et al. Efficient generation and characterization of spectrally factorable biphotons, *Opt. Express* **25**, 7300-7312 (2017).
[S17] Z. Zhang, J. Mower, D. Englund, F. N. C. Wong, and J. H. Shapiro, Unconditional security of time-energy entanglement quantum key distribution using dual-basis interferometry, *Phys. Rev. Lett.* **112**, 120506 (2014).
[S18] C. K. Hong, Z. Y. Ou, and L. Mandel, Measurement of subpicosecond time intervals between two photons by interference, *Phys. Rev. Lett.* **59**, 2044 (1987).
[S19] Y. J. Lu, R. L. Campbell, and Z. Y. Ou, Mode-locked two-photon states, *Phys. Rev. Lett.* **91**, 163602 (2003).
[S20] Z. Xie, et al. Harnessing high-dimensional hyperentanglement through a biphoton frequency comb, *Nat. Photonics* **9**, 536-542 (2015).
[S21] K.-C. Chang, et al. High-dimensional energy-time entanglement up to 6 qubits per photon through biphoton frequency comb, in *Conference on Lasers and Electro-Optics*, OSA Technical Digest, Optical Society of America, paper JTu3A.6 (2019).
[S22] V. Giovannetti, L. Maccone, J. H. Shapiro, and F. N. C. Wong, Generating entangled two-photon states with coincident frequencies, *Phys. Rev. Lett*. **88**, 183602 (2002).
[S23] O. Kuzucu, F. N. C. Wong, S. Kurimura, and S. Tovstonog, Joint temporal density measurements for two-photon state characterization, *Phys. Rev. Lett.* **101**, 153602 (2008).
[S24] C. Chen, et al. Indistinguishable single-mode photons from spectrally-engineered biphotons, *Opt. Express* **27**, 11626-11634 (2019).
[S25] B. M. Terhal, and P. Horodecki, Schmidt number for density matrices, *Phys. Rev. A* **61**, 040301 (2000).
[S26] J. H. Eberly, Schmidt analysis of pure-state entanglement, *Laser Phys.* **16**, 921-926 (2006).

[S27] J. Mosley, J. S. Lundeen, B. J. Smith, and I. A. Walmsley, Conditional preparation of single photons using parametric downconversion: a recipe for purity, *New J. Phys*. **10**, 093011 (2008).
[S28] J. A. Jaramillo-Villegas, et al. Persistent energy–time entanglement covering multiple resonances of an on-chip biphoton frequency comb, Optica 4, 655-658 (2017).
[S29] K. Zielnicki, et al. Joint spectral characterization of photon-pair sources, *J. Mod. Optics* **65**, 1141-1160 (2018).
[S30] X. Cheng, et al. Design of spontaneous parametric down-conversion in integrated hybrid Si_xN_y-PPLN waveguides for high-dimensional qubit entanglement, *Opt. Express* **27**, 30733-30787 (2019).